RESEARCH ARTICLE

Key Points:
- Anatomy of a major upwelling filament down to submesoscale range
- Comparison with other filaments and generation mechanisms involved
- Implications for carbon export and sinking

Correspondence to:
P. Sangrà,
pablo.sangra@ulpgc.es

The Cape Ghir filament system in August 2009 (NW Africa)

Pablo Sangrà[1], Charles Troupin[2], Beatriz Barreiro-González[3], Eric Desmond Barton[3], Abdellatif Orbi[4], and Javier Arístegui[1]

[1]Instituto de Oceanografía y Cambio Global, Universidad de Las Palmas de Gran Canaria, Las Palmas, Spain, [2]Sistema d'observació i predicció costaner de les Illes Balears, Palma de Mallorca, Spain, [3]Departamento de Oceanografía, Instituto Investigaciones Marinas, Consejo Superior de Investigaciones Científicas, Vigo, Spain, [4]Institut National de Recherche Halieutique, Casablanca, Morocco

Abstract In the framework of the Canaries-Iberian marine ecosystem Exchanges (CAIBEX) experiment, an interdisciplinary high-resolution survey was conducted in the NW African region of Cape Ghir (30°38′N) during August 2009. The anatomy of a major filament is investigated on scales down to the submesoscale using in situ and remotely sensed data. The filament may be viewed as a system composed of three intimately connected structures: a small, shallow, and cold filament embedded within a larger, deeper, and cool filament and an intrathermocline anticyclonic eddy (ITE). The cold filament, which stretches 110 km offshore, is a shallow feature 60 m deep and 25 km wide, identified by minimal surface temperatures and rich in chlorophyll *a*. This structure comprises two asymmetrical submesoscale (∼18 km) fronts with jets flowing in opposite directions. The cold filament is embedded near the equatorward boundary of a much broader region of approximately 120 km width and 150 m depth that forms the cool filament and stretches at least 200 km offshore. This cool region, partly resulting from the influence of cold filament, is limited by two asymmetrical mesoscale (∼50 km) frontal boundaries. At the ITE, located north of the cold filament, we observe evidence of downwelling as indicated by a relatively high concentration of particles extending from the surface to more than 200 m depth. We hypothesize that this ITE may act as a sink of carbon and thus the filament system may serve dual roles of offshore carbon export and carbon sink.

1. Introduction

Upwelling filaments are typical features of the four eastern boundary upwelling systems (EBUS). They consist of narrow (O (10 km)), elongated (O (100 km)) structures of cold water extending offshore in the upper surface layer (O (100 m)), often located near irregularities of the coastline [*Haynes et al.*, 1993]. They are recurrent structures identifiable by low surface temperature and high chlorophyll *a* concentration signals.

Filaments were first recognized several decades ago in the California Current Upwelling System in satellite images [e.g., *Bernstein et al.*, 1977; *Flament*, 1985] and in situ measurements [e.g., *Brink*, 1983; *Brink et al.*, 1984; *Mooers and Robinson*, 1984]. They were investigated in a series of intensive, multidisciplinary projects off the U.S. west coast, including the Coastal Ocean Dynamics Experiment in 1981–1982 [*Kosro and Huyer*, 1986; *Beardsley and Lentz*, 1987], the Coastal Transition Zone program in 1987–1988 [*Brink and Cowles*, 1991, and the related papers in the same issue], and the Eastern Boundary Current experiment in 1993 [*Huyer et al.*, 1998]. These programs helped to define the characteristic spatial and temporal scales of filaments and provided an observational basis for the formulation of hypotheses on their formation mechanism.

The Canary Current Upwelling System includes two major permanent filaments: the Cape Ghir filament and the Cape Blanc Giant filament [*Gabric et al.*, 1993; *Pelegrí et al.*, 2005]. The Cape Ghir filament is located near 31°N (Figure 1), whereas the Cape Blanc Giant filament at 20°N constitutes the southern limit of this system in summer [*Gabric et al*, 1993]. Both filaments occur rooted to major capes; however, their natures are very distinct: the Cape Blanc Giant filament is located at the southern boundary of the subtropical gyre and its origin lies in the separation of the alongshore flow of the Canary Current from the coast at Cape Blanc [*Mason et al.*, 2011]. It coincides with the convergence of North Atlantic and South Atlantic central waters at the Cape Verde Frontal System [e.g., *Zenk et al.*, 1991; *Pérez-Rodríguez et al.*, 2001; *Meunier et al.*, 2012]. *Troupin et al.* [2012] proposed the origin of the Cape Ghir filament in injection of cyclonic relative vorticity by

the surface wind curl in the region of the coastal upwelling jet. This wind vorticity source disturbs the existing potential vorticity balance of the upwelling jet, preventing it from continuing southward and detaching it from the coastal region to give rise to the filament. Other mechanisms have been proposed for filament generation such as interaction of the upwelling jet with the topography [*Ikeda and Emery*, 1984; *Strub et al.*, 1991; *Hagen et al.*, 1996], baroclinic instability [*Ikeda and Emery*, 1984], meandering of the upwelling jet [*Strub et al.*, 1991], interaction with a field of synoptic-mesoscale eddies [*Strub et al.*, 1991; *Peliz et al.*, 2004; *Meunier et al.*, 2012], and influence of the wind [e.g., *Kelly*, 1986; *Hagen et al.*, 1996; *Castelao and Barth*, 2007].

The earliest of the few in situ studies conducted on the Cape Ghir filament [*Hagen et al.*, 1996] was based on Conductivity, Temperature, and Depth (CTD) observations. The filament was described as a wide (∼150 km) tongue of cold upwelled water extending about 200 km seaward from the coast between Cape Sim and Cape Ghir and centered at 31°N (Figure 1). The large offshore extension of the filament was attributed to entrainment between two counter-rotating eddies. *Pelegrí et al.* [2005] found, like *Hagen et al.* [1996], that the filament extended from the surface to 150 m depth. They reported an along-filament geostrophic flow of 1.1 SV referenced to 650 db at 31°N. They also observed in two cruises, the signs of an intra-thermocline anticyclonic eddy below the filament and suggested that it may be a recurrent structure linked with the poleward slope undercurrent.

García-Muñoz et al. [2005] surveyed the filament focusing their attention on the carbon exchange. They determined that the Cape Ghir filament was responsible for the export of up to 63% of the total annual primary production of their region of study (the coastal waters between Cape Mazagan 33°15′N and Cape Ghir). *Álvarez-Salgado et al.* [2007] estimated that the export of carbon in Northeast Atlantic filaments may be 2.5–4.5 times greater than that related with the Ekman transport, and that the Cape Ghir filament exports 2–3 times more primary production than the other filaments in the same region.

The above studies were performed with stations 16 km apart, a distance less than half of the climatological first baroclinic Rossby radius of deformation for the region, $Rd \sim 30$ km [*Chelton et al.*, 1998]. Therefore, although they have provided a first view of the filament and its effects, there is a need for finer scale studies in order to reveal the exact nature of the filament and its submesoscale variability (∼10 km). With this aim, an interdisciplinary survey, a finely sampled along track, of the filament was carried out from 16 August to 5 September 2009 in the framework of the Canaries-Iberian marine ecosystem Exchanges (CAIBEX) project. This study aims to provide a physical description of the filament down to the submesoscale range.

2. Sampling and Data Collection

2.1. Sampling

The CABEIX-III interdisciplinary survey of the Cape Ghir filament region took place on board R/V *Sarmiento de Gamboa* in late summer 2009. Hydrographic properties were measured with a combination of conventional Conductivity, Temperature, and Depth (CTD) probe casts at discrete stations, continuous tows of CTD on an undulating vehicle (SeaSoar) over a grid of tracks across the filament, deployments of instrumented drifters, and remote sensing. For this study, data from 7 SeaSoar transects and a CTD transect across the filament core, supported by remotely sensed maps of SST, chlorophyll *a* and 10 m wind, were selected (Figure 1b).

Our sampling strategy was guided by the signal of the filament in the remotely sensed SST field. The SeaSoar sampling was started 200 km from the coast along six meridional transects separated on average by 28 km as they approached the coast (Figure 1b). The transects were numbered 1–6 from west to east and were conducted from 17 August to 20 August (Table 1). The easternmost line along 10°35′N was repeated on 22 August (Transect 7) with the objective of locating and confirming the position and scales of the filament. The same transect was sampled again on 26–27 August with 13 CTD stations approximately 9 km apart in order to sample the physical and biogeochemical properties of the filament (T_1–T_{13} in Figure 1b). The horizontal resolution of the gridded fields from SeaSoar and CTD transects is about 4 and 9 km, respectively, well below $Rd \sim 30$ km and thus able to resolve the submesoscale. Note that this resolution applies only in the along-transect direction since the coarse separation between them (28 km) precludes consideration of zonal submesoscale variability. Transects 1–6 were sampled in 3 days and so may be considered as
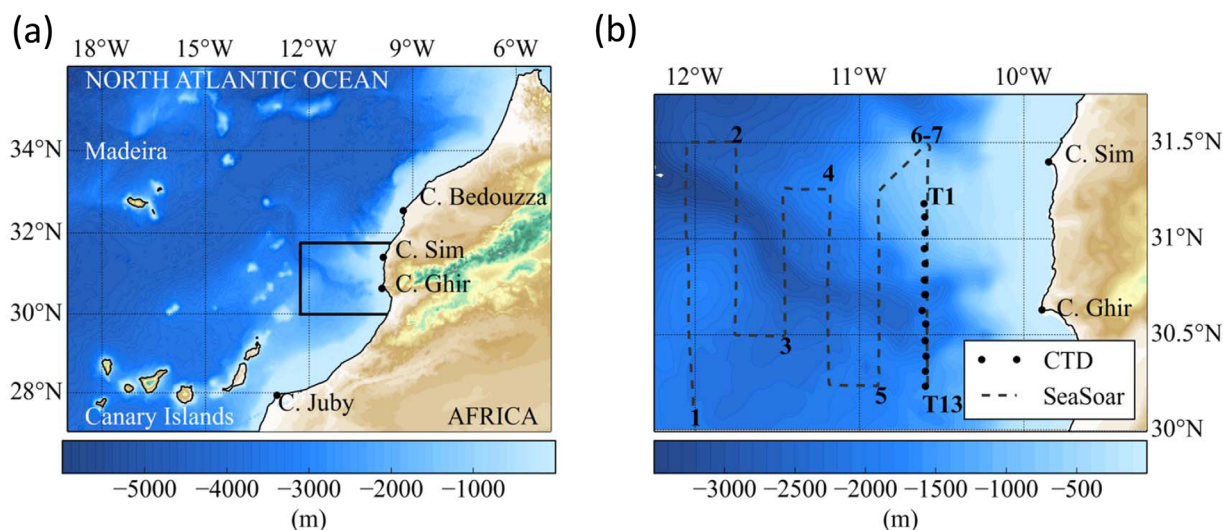
Figure 1. (a) Bathymetry of the observational domain. (b) SeaSoar survey (dashes) and CTD station (black circles) locations. SeaSoar meridional transects are numbered from 1 to 7 starting from the west.

quasisynoptic. As mentioned, the transect along 10°35′W was repeated three times as Transect 6, Transect 7 and the CTD section in a time interval of a week, thus following the temporal variability of the filament.

2.2. Data Collection

We used a SeaSoar Mk II towed vehicle equipped with a CTD SB911+. In most profiles, the SeaSoar measurements extend from 30 m down to 400 m. On average, the profiles were separated horizontally by 4 km with an effective vertical resolution of 72 cm. Along 10°35′N, 13 CTD casts were made to a nominal depth of 500 m (Table 1) using a SB911+ instrument additionally equipped with a Seapoint Chlorophyll Fluorometer, dual SBE43 oxygen sensors, Wetlabs C-Star Transmissometer (25 cm 660 nm), Seapoint Turbidity Meter, and Biospherical Remote Photoradiometer sensors. Raw data files were processed with Sea-Bird SEASOFT software (http://www.seabird.com/software/softrev.htm) and vertically averaged into 1 m bins.

Current velocities were measured continuously using two synchronized hull-mounted RDI_ADCP Ocean Surveyor, working at 75 and 150 kHz. The 75 kHz ADCP provided raw data with 5 min ensembles from the surface to ∼800 m and a bin size of 16 m. The 150 kHz broadband ADCP provided raw data with 5 min ensembles from the surface to ∼300 m with a bin size of 4 m. The raw data were quality controlled, corrected for heading misalignment, and edited with the Common Oceanographic Data Access System [CODAS, *Firing et al.*, 1995]. On average, the processed profiles provide good data from 20 to 200 m for the 150 kHz ADCP and from 60 to 700 m for the 75 kHz ADCP.

Chlorophyll *a* (Chl *a*) concentrations were estimated fluorometrically by means of a Turner Designs bench fluorometer, previously calibrated with pure Chl *a* (Sigma Co.), according to *Holm-Hansen et al.* [1965]. Seawater samples (500 mL) were filtered through Whatman GF/F filters. Pigments were extracted in cold acetone (90% vol/vol) for 24 h. The relation between the voltage readings obtained with the fluorometer (F) and the Chl *a* concentrations from extracted pigments [Chl *a* (mg m^{-3}) = 2.159F + 0.026; R^2 = 0.96] was used to transform in situ fluorescence to actual Chl *a*.

Table 1. CAIBEX Sampled Transects Characteristics

Transect	Date (2009)	Longitude W	Distance (km)	Depth (m)	Dives/Casts
Transect 1	17 Aug	12°03′	139	400	30
Transect 2	18 Aug	11°45′	111	400	25
Transect 3	18 Aug	11°27′	83	400	20
Transect 4	19 Aug	11°11′	111	400	25
Transect 5	19 Aug	10°53′	111	400	25
Transect 6	20 Aug	10°35′	139	400	30
Transect 7	22 Aug	10°35′	139	400	30
CTD section	26–27 Aug	10°35′	111	550–2020	13

SST data files were downloaded from the U.S. National Oceanographic Data Center at ftp://data.nodc.noaa.gov/pub/data.nodc/ghrsst/L2P/. The products selected are the GHRSST-PP L2P near Atlantic Regional (NAR) 17 and 18, originally produced by the ESA Medspiration project (www.medspiration.org/). The swath with the best spatial coverage is selected between the ascending/descending swaths from NOAA-17/NOAA-18 satellites. This selection criterion leads to images obtained at different times of the day, but the resulting diurnal effect is not a concern since the filament is identified from the temperature gradients. Furthermore, the wind was quite strong during the field work (>6 m s^{-1}), so that the diurnal effects are limited. In the study region (Figure 1) and period (15 August to 31 October 2009), the cloud coverage varied strongly from 1 day to another. The average cover was about 50%, while only 13% of the images had less than 25% cloud cover. Some pixels were contaminated by clouds, but also by dust input from the nearby Sahara desert.

The Moderate Resolution Imaging Spectroradiometer (MODIS) sensor on board Aqua and Terra satellites provides Chl a concentrations with a 1 km spatial resolution for the level 2 data and 4 km resolution for the level 3 data (uniform space-time grid scales). Data are obtained from the Ocean Color server at http://ocean-color.gsfc.nasa.gov [*Feldman and McClain*, 2010]. For the individual images, the satellite (Aqua or Terra) providing the best spatial coverage was selected. For the composite image, all the level 3 images were combined.

Along-transect ocean surface winds at 10 m height are measured by the SeaWinds Scatterometer of the QuikSCAT satellite mission with a resolution of 12.5 km. The SeaWinds scatterometer on board, the QuikScat satellite performs two daily (ascending and descending) passes on a single location to fulfill 14 swaths. Data files were acquired from the Physical Oceanography Distributed Active Archive Center (PODAAC) of the Jet Propulsion Laboratory (JPL) at ftp://podaac-ftp.jpl.nasa.gov/allData/quikscat/L2B12/. Each daily map was produced by combining the 14 swaths of the satellite.

3. The Cold and Cool Filaments

The signature of the filament off Cape Ghir is clearly evident in the surface maps as a cool, chlorophyll-rich tongue that stretches zonally offshore from the coastal upwelling. The filament structure consists of a relatively narrow (~20 km wide and 100 km long) and colder (T $<$ 19°C) core region embedded within the southern part of a broader (~120 km) cool (19°C $<$ T $<$ 21°C) structure, as seen on 27 August (Figure 2a). The temperature difference between the filament and the surrounding unperturbed oceanic water reaches up to 4°C. The southern boundaries of the core and the cool embracing region coincide, as shown by the sharp temperature gradients, whereas the northern boundary of the cool surrounding region is located well north of the core, near Cape Sim.

These two different regions of the filament are also recognizable in the Chl a satellite image of 27 August (Figure 2b), where a narrow, hook-shaped filament of higher Chl a concentration originating near Cape Ghir coincided with the cold core of the filament within a broader region of elevated Chl a concentration. Although the SST signature of the filament varied in intensity and position during the cruise period, its dual structure was observed in the majority of available SST images. The averaged SST field from these images (Figure 2c) confirms the persistence of the dual structure, despite the possibility of bias from cloud cover and smoothing of the spatial variability. In this averaged field, a relatively narrow core cold region is centered on Cap Ghir within a warmer and broader region extending from Cape Ghir to Cape Sim. These regions of the Cape Ghir structure will be denoted as the inner small "cold filament" and the surrounding larger "cool filament," respectively. As discussed in section 7.3, this dual structure of the filament does not imply two independent filaments, simply that the filament may be viewed as a broad area of upwelled water (cool filament) with its most intense surface manifestation along a narrow axis (cold filament). During the cruise period, QuickSCAT wind data over the survey domain (30°N–31.45′N, 11°30′W–9°W) were quite homogeneous with a strong meridional component. The mean wind speed and direction were 6 m s^{-1} and northeasterly, respectively, thus inducing upwelling favorable wind stress (Figure 3).

4. Cold Filament Region and Subsurface Anticyclonic Eddy

Figure 4 shows potential temperature, salinity, and velocity sections for the CTD transect crossing the filament along 10°36′W. As seen in the corresponding SST field, this section, 120 km long, crossed the cold
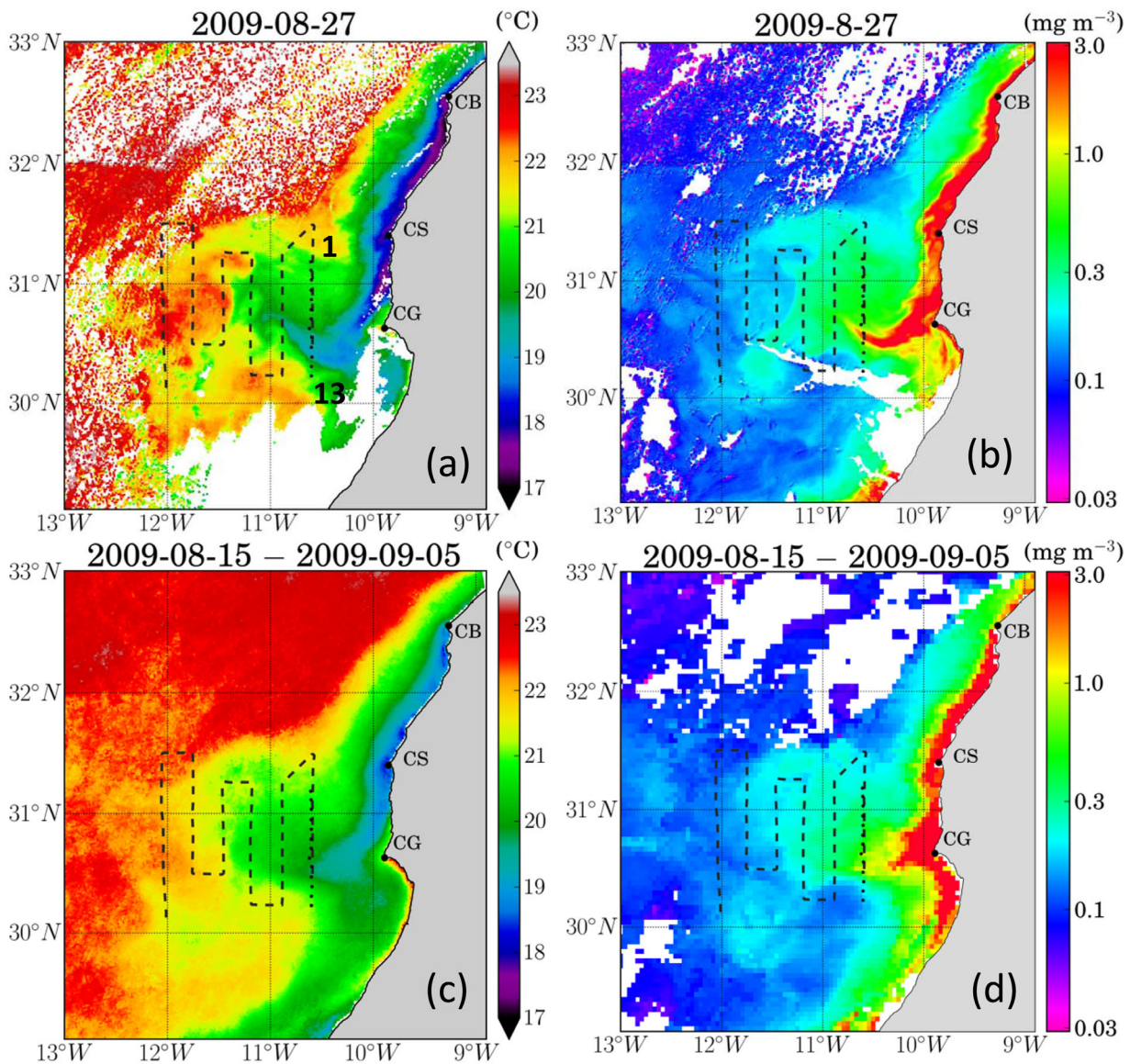
Figure 2. (top) Selected day and (bottom) averaged (left) SST and (right) chlorophyll *a* fields as obtained from remote sensed data. Cape Chir (CG), Cape Sim (CS), and Cape Bedouzza (CB) are indicated. Dashed line indicates SeaSoar transects and black dots CTD stations.
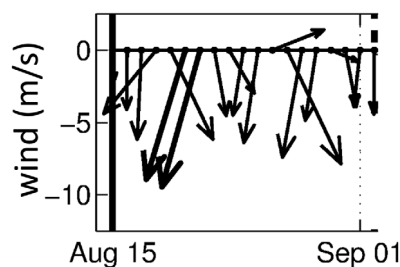

Figure 3. Daily wind vectors obtained by averaging the QuikSCAT measurements over the domain 30°N–31°45′N, 11°30′W–9°W. Winds stronger than 10 m s^{-1} are indicated by bold arrows.

filament and much of the surrounding cool filament (Figure 2a). The cold filament signature is clearly recognizable in the potential temperature section by the isotherms doming in the near-surface layers above ~60 m depth (Figure 4b). Below 60 m, isotherms, e.g., 16°C, show a broader doming across almost all the section outside the cold filament. This doming, the signature of the broader, cool filament extends to ~150 m depth. The inner cold filament is thus shallower (60 m versus 150 m, respectively) and narrower (25 km versus 120 km, respectively) than the cool filament. Therefore, the cold filament may be viewed as a freshly upwelled feature superimposed on the cool filament. As seen in Figure 4a, the depth range of the cold filament is occupied by a broad salinity minimum limited by the 36.4 isohaline. This homogeneous low salinity layer is connected below with a
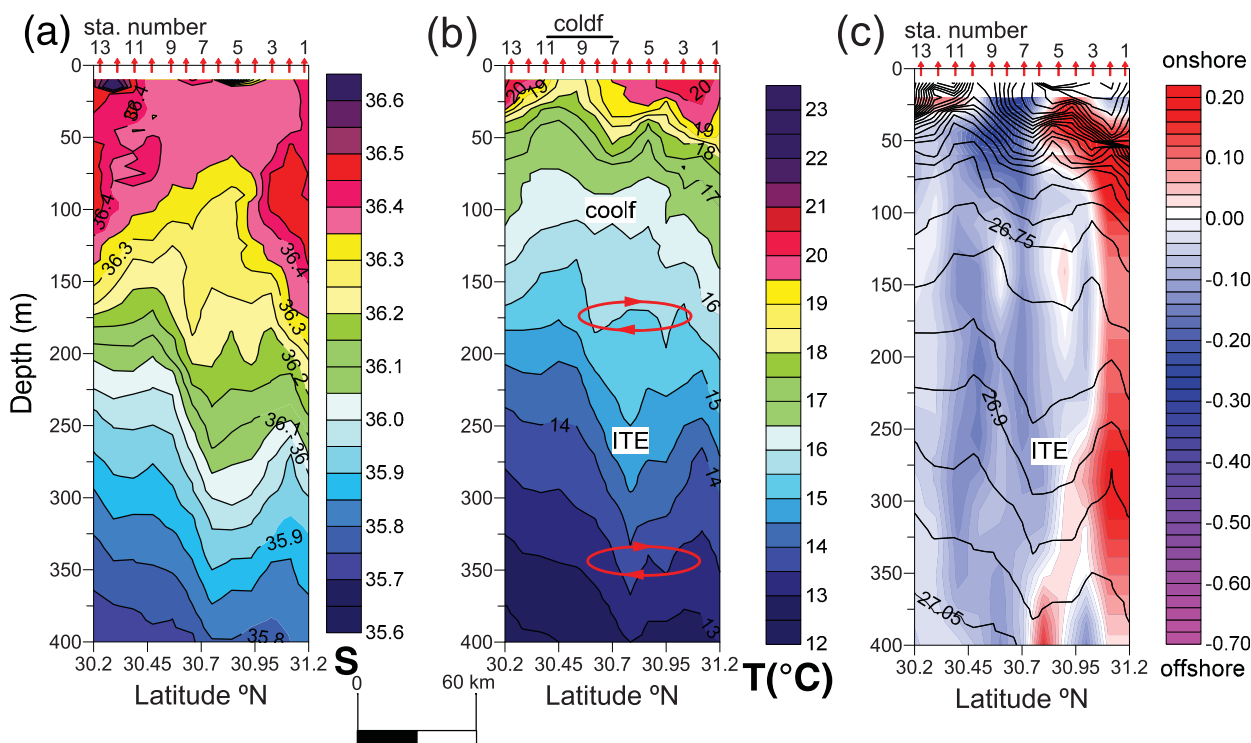
Figure 4. CTD transect across the cold filament at 10°36′W carried out on 26–27 August 2009 (see Figure 1b for location). (a) Salinity, (b) potential temperature, (c) 150 and 75 kHz ADCP cross-transect velocity, black contour lines are potential density anomaly isopycnals (kg m^{-3}). Location of the cold filament (coldf), cool filament (coolf), intrathermocline eddy (ITE), and related circulation are indicated in Figure 4b. Red ellipses in Figure 4b indicates the ITE-related anticyclonic circulation.

narrower doming of salinity between 150 and 100 m and a narrow zone of northward plunging isohalines and isotherms at stations 6–10.

An offshore flowing current jet of submesoscale width (∼18 km) between stations 9 and 7 was associated with the northern front of the cold filament as indicated by potential density anomaly (Figure 4c). Speeds of up to 0.3 m s^{-1} were measured by the 150 kHz ADCP between the uppermost available bin at 20 and 60 m depth. The southern front of the cold filament, located between stations 11 and 13, was associated with a similar, but shoreward flowing, submesoscale jet-like structure. It was much shallower and weaker, reaching to only 30 m with a maximum speed of 0.1 m s^{-1}. However, the occurrence of such weak onshore flow must be taken with caution as values are close to the order of magnitude of the error according to the ADCP specifications. Therefore, the cold filament exhibits a clear asymmetry with an intense northern front transporting water offshore and a weak southern front transporting water onshore. The related relative vorticity field in this cold filament is therefore strongly positive (cyclonic).

At and north of the cold filament's northern front, the isolines below 150 m and between stations 9 and 2 deepened to form a bowl-like structure that reached 500 m depth, although data are displayed only to 400 m depth (Figure 4). The velocity section shows that this structure is associated with an anticyclonic circulation that extends from the deeper levels up to the surface (Figure 4c). This structure was also observed along SeaSoar Transects 5, 6, and 7 in the same depth range except in Transect 5 where the signal was detected only to 250 m (Figures 5c–5e). Transects 6 and 7 crossed the filament near the same location as the CTD section but 7 and 4 days earlier, respectively. Transect 5 crossed the filament also but 30 km west of Transect 6 and several hours earlier (Figure 1b). The anticyclonic circulation reached the uppermost ADCP bin at 60 m in Transects 6 and 7 (Figures 5d and 5e) but only 250 m depth in Transect 5 (Figure 5c). This structure is consistent with an intrathermocline anticyclonic eddy (ITE) of diameter >70 km and a thickness of ∼300 m that did not extend as far as Transect 4, located 30 km to the west of Transect 5. The anticyclonic deflection of the SST and Chl *a* structures of the cold filament seen in Figures 2a and 2b may be related to the presence of the ITE. The broad salinity minimum observed in the upper layers of the CTD section (Figure 4a) may also have its origin in the entrainment by the ITE of low salinity waters upwelled
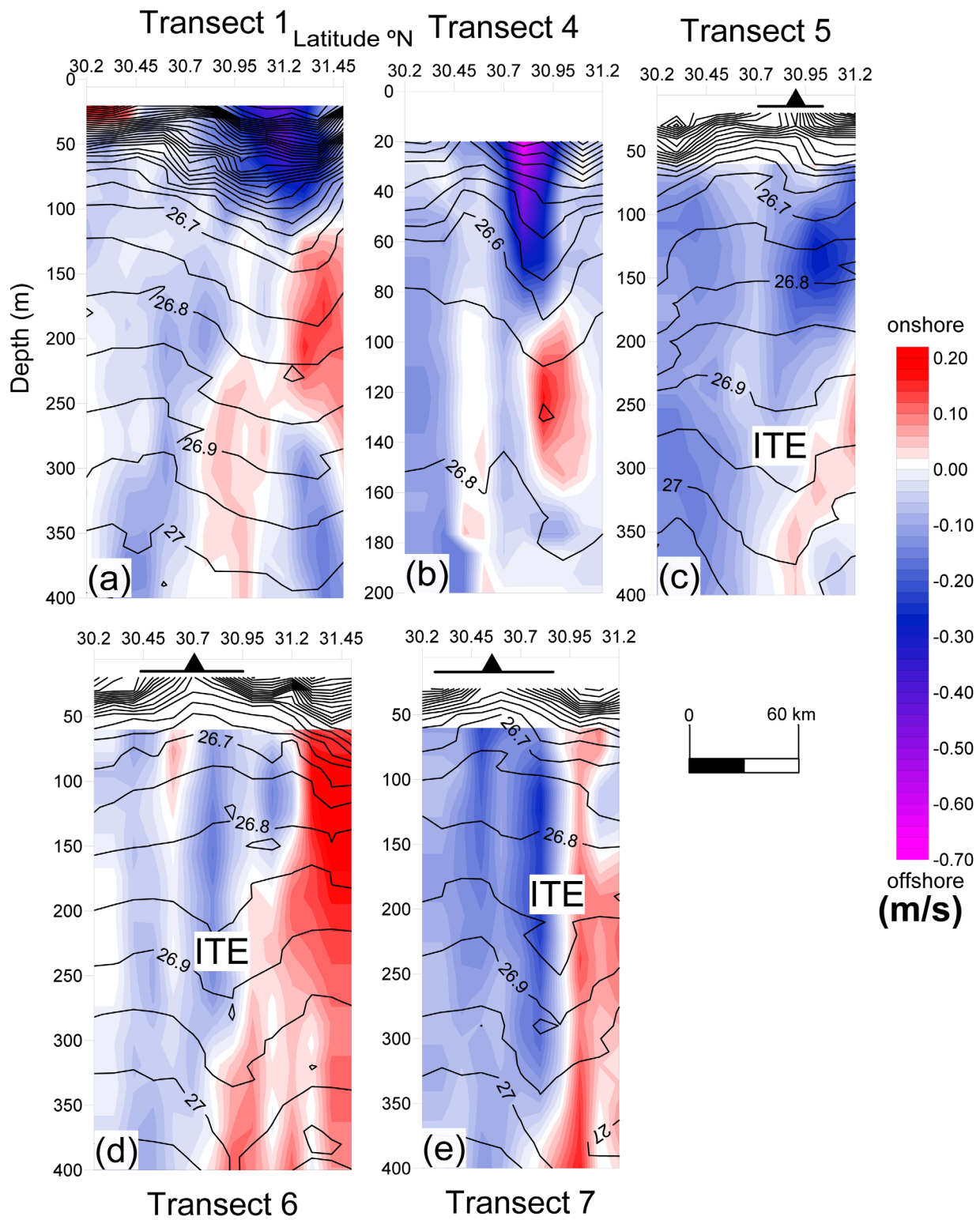
Figure 5. ADCP sections across the SeaSoar transects, with potential density anomaly isopycnals superimposed on the velocity field: (a) merged 150 kHz and 75 kHz ADCP velocities, (c–e) 75 kHz ADCP velocities, while (b) 150 kHz ADCP velocities. Location and extension of the cold filament are annotated in the bottom figures by a black triangle and by a straight line, respectively.

upstream. Where the ITE anticyclonic circulation reaches the surface layers, it will interact with the offshore flow of the cool filament. As shown in the case of the CTD section, this leads to a returning jet-like flow that interrupts the offshore flow of the cool filament (Figure 4c). This jet is located north of the northern front of the cold filament, centered at station 5 and extending down to 60 m (Figure 4c).

ITEs are quite common features in the ocean [*Hormazabal et al.*, 2013, and references therein]. They are a particular class of mesoscale anticyclonic eddies characterized by having their core in subsurface waters within the main thermocline [*Gordon et al.*, 2002; *Hormazabal et al.*, 2013]. Their most remarkable feature is the associated dome shape of the isopycnals in the shallower layers and bowl shape in the deeper layers forming thus lens-like structures overall [*Kostianoy and Belkin*, 1989; *Nauw et al.*, 2006; *Johnson and McTaggart*, 2010; *Hormazabal et al.*, 2013]. However, in the case of the Cape Ghir ITE, the dome shape of the upper layers is missing, probably because the interaction with the filament in these layers causes temperature and salinity compensation (Figures 4a and 4b). Another difference is that the Cape Ghir ITE is not composed of homogeneous water as is the case for a typical lens-like ITE.

As mentioned, the SeaSoar Transect 6 crossed the core region of the filament at the same location as the CTD section but 1 week before. The corresponding temperature section indicates that the small, shallow, cold filament, now centered at 30.7°N, had shifted 20 km southward (Figure 6d). The main difference between the two sections is reflected in the salinity distributions. The section along Transect 6 depicts a clear salinity minimum between 150 m and the surface, indicated by a blue triangle in Figure 6a. This minimum is located in the northern front of the cold filament, indicated with a black triangle in Figure 6d. The salinity minimum coincides with the temperature minimum of the surrounding cool filament reflected in the displacements of the 16°C or 17°C isotherms but is much narrower. The salinity minimum coincides with the location of the ITE (Figure 6a), as also seen in the CTD section (Figure 4a). The coincident southward displacements of the cold filament, the salinity minimum, and the position of the ITE in the week elapsed between Transect 6 and the CTD section suggest that the three structures are intimately connected.

The temperature section along SeaSoar Transect 5, 30 km west of and 2 days before Transect 6, shows the signature of the cold filament slightly further north as indicated by a black triangle in Figure 6e. However, both the salinity minimum and the ITE were located at the same latitude as on Transect 6, suggesting that the northward shift of the cold filament between sections was related to its anticyclonic deflection around the ITE, as suggested by the satellite images (Figures 2a and 2b).

The distribution of fluorometer-calibrated Chl *a* concentration in Figure 7a shows a well-defined near-surface maximum in the cold filament between stations 11 and 9, as a result of the along-filament advection of rich coastal upwelled waters (Figure 2b). Just north of the northern front of the cold filament, a deeper second relative maximum is centered on station 6. Beam attenuation coefficient (660 nm) distribution mirrors the Chl *a* distribution in the upper illuminated layers (Figure 7b). A striking feature of the beam attenuation coefficient distribution is the occurrence of a columnar structure over the depth range 50–350 m between stations 10 and 4 (Figure 7b). This is suggestive of a localized region of abundant sinking particles possibly caused by settling and/or water subduction by downwelling. As this column is not related to any local maximum of particles in the near-surface source layers (Figure 7b), downwelling seems the more likely cause. The colocation of this column with the ITE as seen in Figure 7b is compatible with the idea that the ITE originates in the convergence of the near-surface flow and the corresponding downwelling associated with the straining of the velocity. Another plausible hypothesis that should not be discarded is that particles are being drawn from nearshore.

5. Offshore Subduction and Cool Filament Structure

The signal of the cool filament was evident along Transect 1 in the subsurface layers, centered at 30.5°N in the southern portion of the section (Figure 6c). There, it extended as deep as 250 m and reached horizontally from at least 30.2°N to 30.95°N (~83 km). Comparison of salinity sections along Transects 6, 5, and 1 indicates deepening by ~30 m of the isohalines between 36.4 and 36, suggesting the subduction of the filament. The structure of the salinity field for Transect 1, similar to that in the other sections, consisted of a broad low salinity region with an embedded narrow salinity minimum at the center of the cool filament. As for the case of the CTD section, the narrow salinity minimum did not reach the near-surface layers. The
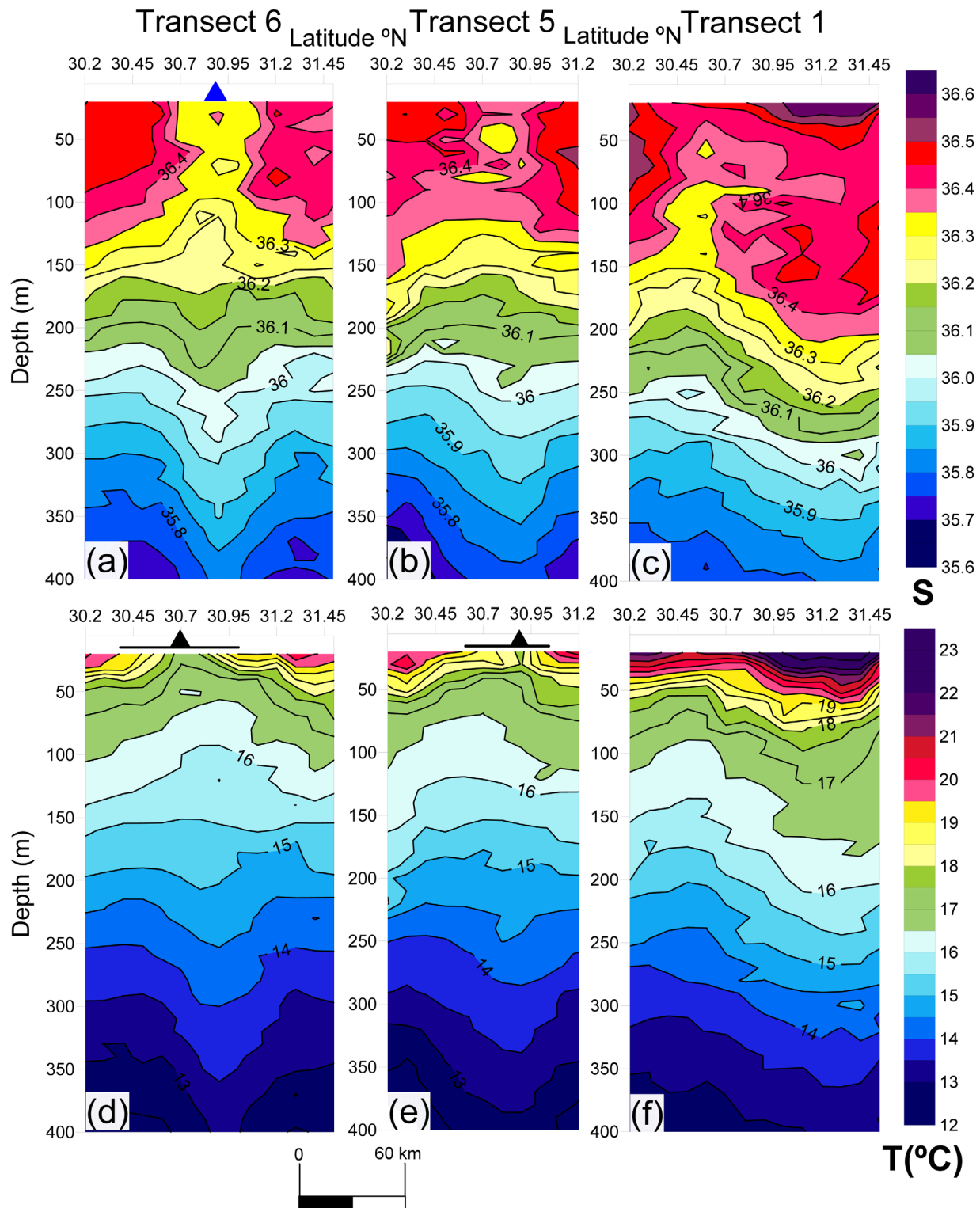
Figure 6. (top, a–c) Salinity and (bottom, d–f) potential temperature sections along meridional SeaSoar Transects 6, 5, and 1(see Figure 1b for positions). Location and extension of the cold filament are annotated in the bottom figures by a black triangle and by a straight line, respectively. Blue triangle in Figure 6a indicates the location of the salinity minimum.

signal of the cool filament is also recognizable in the temperature field through the doming of the isotherms and associated shoaling of the thermocline and mixed layer between 30.2°N and 31.2°N (Figure 6f). In Transect 1, the cold "core filament" was no longer visible.
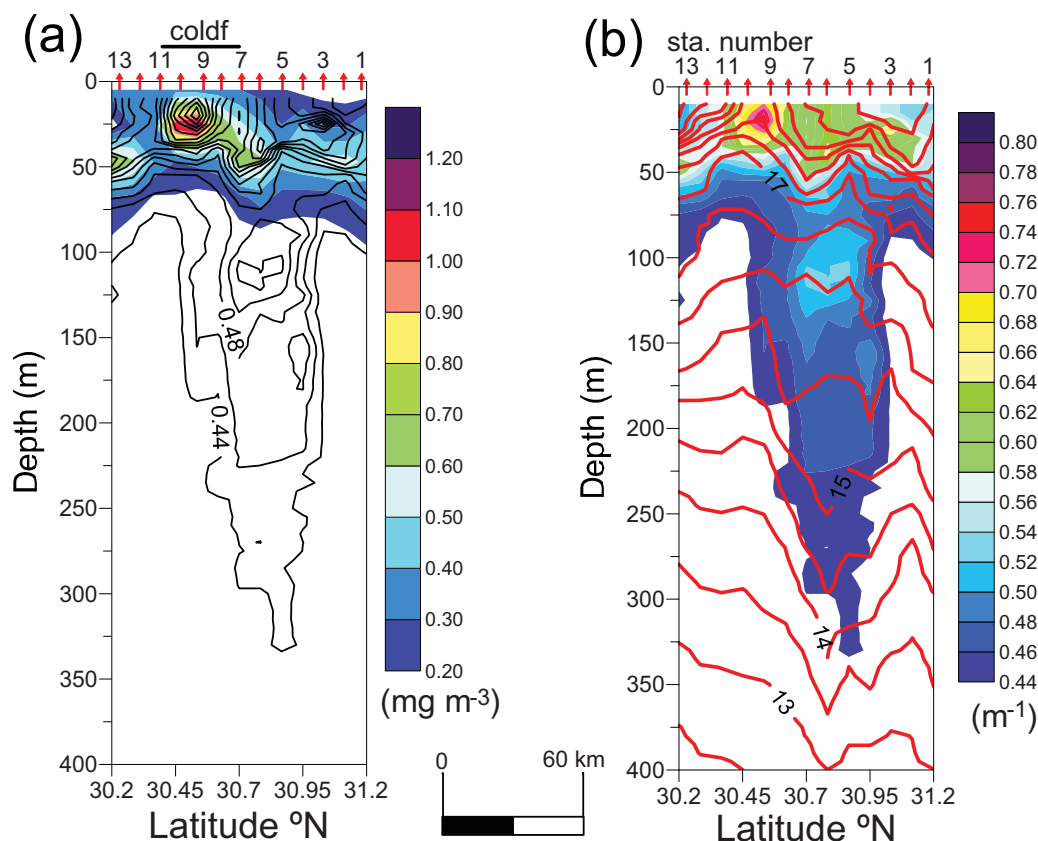
Figure 7. Vertical sections along the 10°38'N CTD transect. (a) Fluorometer-calibrated chlorophyll *a* concentration (color filled contour plot) superimposed on the transmissometer beam attenuation coefficient isolines (black contour lines). Data below 0.13 mg m^{-3} are blanked. (b) Transmissometer beam attenuation (color filled contour plot) coefficient superimposed on potential temperature isotherms in °C (red contour lines). Data below 0.44 m^{-3} are blanked.

North of the cool filament doming, between 30.95°N and 31.45°N, isotherms showed troughs associated with a local surface temperature maximum at 31.2°N, which is also reflected in a bowl-like structure in the isopycnals distribution (Figure 5a). The cross-transect velocity component shows that this frontal structure is related to offshore flow at speeds up to 0.4 m s^{-1} in a mesoscale jet 55 km wide and 100 m deep. Below the jet, between 100 and 200 m depth, a return flow also exhibits jet-like structure. Isopycnals along Transect 4 (Figure 5b) show a similar bowl structure between 30.7°N and 31°N (∼30 km) associated with a stronger mesoscale jet flowing offshore at up to 0.7 m s^{-1}. As for Transect 1, below the jet, a less intense jet-like return flow extended from 90 to 160 m. The surface and subsurface jets and the related bowl-like structure in the isopycnals constitute the northern frontal region of the cool filament.

Where the cold filament crosses 10°35'W, the signal of the northern frontal boundary is smoothed by the interaction with the ITE (Figures 5d and 5e). In the CTD transect, this boundary is indicated by the slumping of the isopycnals at station 2 from the near-surface layers down to 50 m depth (Figure 4c). In SeaSoar Transects 1 and 4, this downward slope is accompanied by a relatively strong offshore flow (Figures 5a and 5b). Below and south of the slumping isopycnals, the flow reversal down to 400 m is related to the presence of the ITE as shown in Figure 4c. Thus, the ITE and the northern boundary of the cool filament clearly interact to perturb the velocity and potential density fields. This can be also seen in SeaSoar Transect 6 where the cool filament boundary is recognizable through the slumping of the isopycnals down to 120 m between 31.2°N and 31.45°N (Figure 5d).

At the southern end of Transect 1, a narrow, shallow, and weak (<0.2 m s^{-1}) jet flowing inshore between 30.2°N and 30.4° signals the southern boundary of the cool filament region (Figure 5a). As for the case of the cold inner filament, the frontal regions of the cool filament display asymmetry. At the root of the filament, the southern fronts of cold and cool filaments merge together. Unlike the larger cool filament, the cold inner
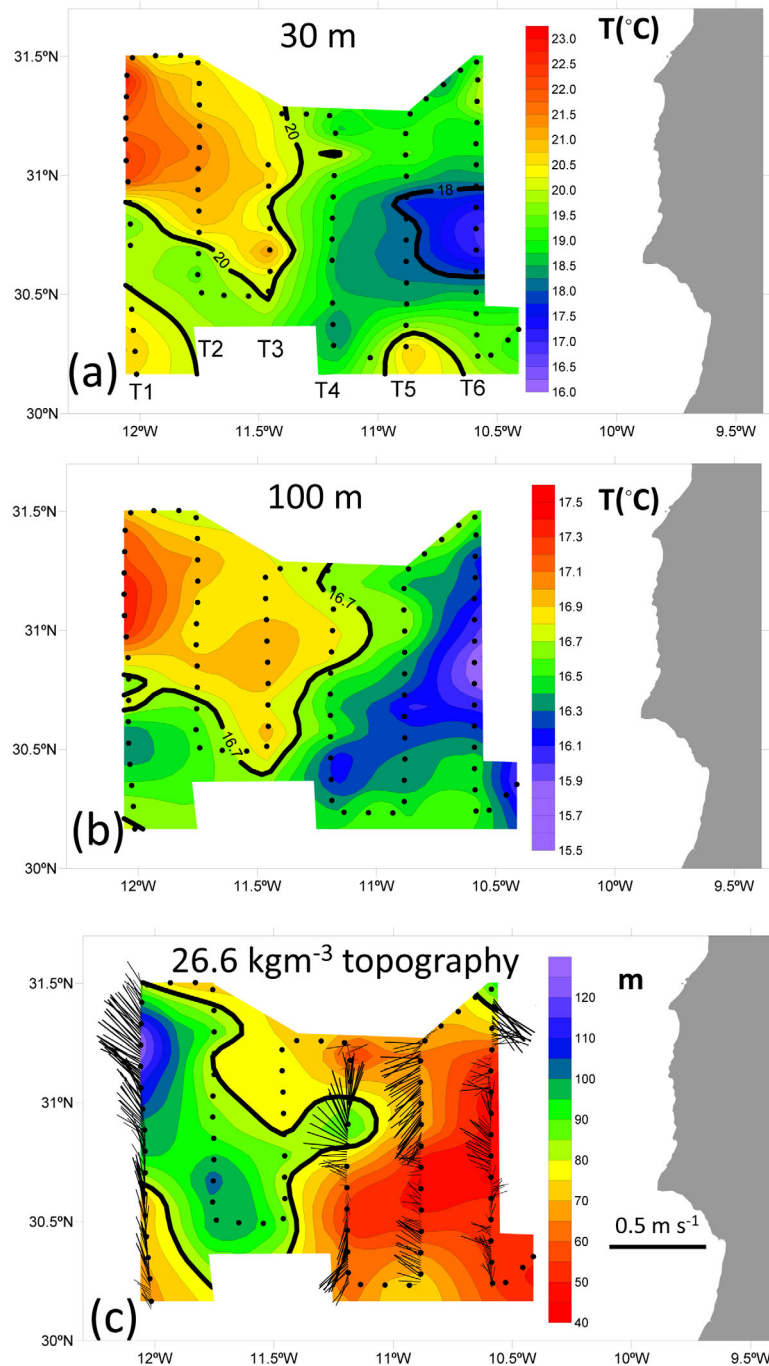
Figure 8. Temperature field at (a) 30 m depth and (b) 100 m depth as obtained from SeaSoar Transects T1, T2, T3, T4, T5, and T6. (c) 75 kHz ADCP velocity averaged from the uppermost bin, 60 m, down to 100 m superposed to 26.6 kg m^{-3} isopycnal topography.

filament was not observed by in situ measurements seaward of Transect 5, 80 km offshore. Neither was the cold filament signal detected beyond 100 km offshore in any of the SST images (e.g., Figure 2a).

6. Filament Signature in the Horizontal Fields

Quasisynoptic horizontal fields obtained by combining SeaSoar Transects 1–6 are shown in Figure 8. Those fields must be viewed with caution since, as pointed out before, the coarse separation between transects (28 km) precludes consideration of zonal mesoscale variability. Keeping this in mind, temperature

distributions at 30 and 100 m depths show the discussed dual structure of the filament in the form of a small, shallow, and cold filament embedded within a larger, deeper, and cool filament. The cool filament signature at 30 m is represented by the broad cool ($18°C < T < 20°C$) region limited by the 20°C isotherm (Figure 8a). The filament appears to be oriented southwestward across lines 6, 5, and 4, but then turns almost 90° to extend northwestward across the outer three lines. At Transect 3, warmer oceanic water ($>20°C$) that occupies the northwest portion of the domain extends south to bound the filament. Transects 3 and 2 were shorter than the others so did not fully capture the filament signature.

The signature of the cold filament is evident in the small cold region ($<18°C$) between transect T6 and T5 embedded within the southern portion of the cool filament. At 100 m depth, the weaker cold filament signature indicates that it is a shallow structure that overlies the cool filament (Figure 8b). Although the signature of the cool filament has weakened at this depth, it is still observable as colder water ($<16.7°C$) stretching westward from the easternmost transects and intruding within the warmer interior ocean water ($>17.6°C$). Comparing the temperature signatures at 30 and 100 m depth, it can be seen how the cool and cold structures represent two different regions of the filament. The cool filament has the same southwestward orientation at both depths whereas the cold filament is a shallow, westward-oriented structure overlying the cool filament.

As it has been discussed above, the filament subducts as it stretches westward. This is supported by the topography of the 26.6 kg m^{-3} depicted in Figure 8c, which shows the signature of the filament sinking as it stretches westward from a start depth of 30 m at the filament root (Transect 1) to 80 m at the filament head (Transect 6). A striking feature already mentioned is that at the northern frontal region of the cool filament the isopycnals were depressed in a bowl shape in Transects 4 and 1 (Figures 5a and 5b). This is reflected in the 26.6 kg m^{-3} topography by the isopycnal trough seen between Transects 1 and 4 (bold line in Figure 8c) that stretches all along the northern boundary of the filament. Notice that "bull's-eyes" of minimum depth inside this region are an interpolation artifact due to coarser separation between transects and it may be expected that this feature is continuous all along this frontal region.

Figure 8c also shows the velocity field along Transects 1, 4, 5, and 6 from the 75 kHz ADCP data, averaged from the uppermost bin, 60 m, down to 100 m. Data along Transect 2 and 3 were discarded because of disagreement between the 75 and 150 kHz ADCP data sets, both of which functioned intermittently during more half the length of these transects. Although there is an overall offshore flow associated with the filament, the velocity field shows high variability between and along transects. At the head of the filament in Transect 1, the flow is oriented northeast parallel to the orientation of the filament as shown in Figures 8a and 8b. North of the transect, there is a clearly increase of the flow coinciding with the isopycnal trough that constitutes the northern frontal region of the cool filament. In Transect 4, this depressed frontal region also coincides with stronger flow. The flow pattern presents strong divergence coincident with the region where the filament meets with warmer interior ocean waters (Figure 8a). At Transect 5, the flow is quite uniformly westward except at the axis of the filament where it is very weak. This diminution of the flow near the axis of the filament, also visible in Transects 4 and 6, will introduce a relative cyclonic vorticity at the axis of the filament as already mentioned. The flow is highly variable in Transect 1 due to the occurrence of the cold filament and the ITE. In this regard, notice the relatively strong return flow at the northward end of the transect related to the presence of the ITE as seen in Figure 5d.

7. Discussion

7.1. Origin and Importance of the ITE

Our observed cool filament region corresponds closely in position and extent with the broad filament signal observed from low resolution in situ data by *Hagen et al*. [1996] and *Pelegrí et al*. [2005]. These last authors also reported the signature of a subsurface anticyclonic eddy-like structure below the cool filament. As they observed this signal in two cruises, they suggested that it may be a recurrent structure. Observations of a similar feature in the present study add evidence for a link between the eddy and the occurrence of the filament, and it may be viewed as forming part of the filament system.

Pelegrí et al. [2005] proposed that the Cap Ghir ITE may be connected to the poleward slope undercurrent. ITEs linked with poleward slope undercurrents observed in other eastern boundary upwelling systems clearly show nearly homogeneous oxygen minimums. [*Cornuelle et al*., 2000; *Garfield et al*., 1999, 2001;
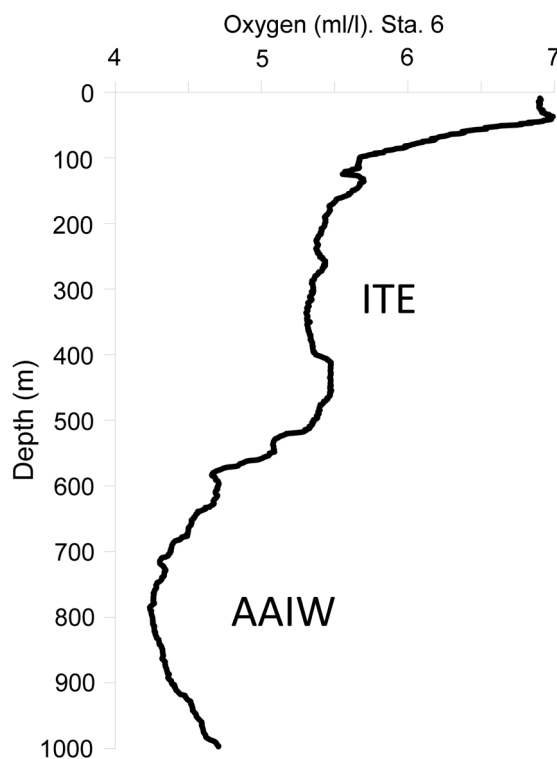
Figure 9. Oxygen profile for station 6 of the CTD transect located at the ITE center. ITE and AAIW indicate the location of the intrathermocline eddy and the low oxygen Antarctic Intermediate Water, respectively.

Hormazabal et al., 2013]. *Machín et al.* [2006] observed along a zonal section near Cape Ghir that in summer the poleward slope undercurrent is located between 600 m and the bottom, much deeper than those related with the California Current Upwelling System or the Chile-Peru Upwelling System which are centered at 300 m depth [e.g., *Collins et al.*, 2000; *Hormazabal et al.*, 2013]. Observations by *Vélez-Belchi et al.* [2012] confirm the occurrence of such a deep poleward slope undercurrent that near Cape Ghir was related to a nearly homogeneous salinity minimum, S < 35.4, corresponding to Antarctic Intermediate Water (AAIW). In a few deep casts made over the slope during the study, we observed this homogeneous minimum salinity layer well below the anticyclonic structure, between 600 and 900 m, coinciding with the depth range for the de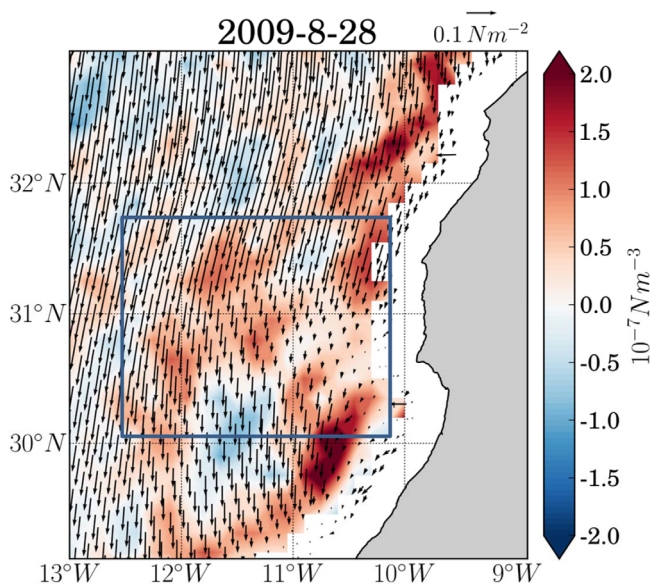ep poleward slope undercurrent reported by *Machín et al.* [2006]. This difference in depth between the observed ITE and the poleward slope undercurrent and the contrast in salinity values between the ITE (North Atlantic Central Water S >35.4) and the slope current (AAIW S < 35.4) suggests no connection between the two. Moreover, AAIW is easily identifiable by an oxygen minimum, the occurrence of such minimum related to AAIW deep poleward flow was observed just below the ITE as depicted in Figure 9.

As already advanced the colocation of the apparent downwelling suggested by high beam attenuation with the ITE (Figure 7b) is compatible with the idea that this eddy may originate in the near-surface flow convergence and the corresponding downwelling associated with the straining of the velocity field. This secondary circulation in the filament may compress the planetary vorticity tubes to act as a source of anticyclonic relative vorticity and thus form the ITE. Therefore, the working hypothesis is that the ITE is intrinsically linked to the filament system rather than being an independent structure arising from the poleward slope undercurrent. The low light transmission core at the ITE suggests that it may represent a region of sinking particles and hence of carbon loss from the upper layers. We propose that the Cape Ghir filament constitutes not only a source of carbon for the interior ocean as reported by other authors [*Álvarez-Salgado et al.*, 2007] but also a localized sink associated with the ITE.

7.2. Self-Induced Nonlinear Ekman Suction and Generation Mechanisms

Mesoscale variability of SST may induce perturbations in the surface wind stress [*Small et al.*, 2008; *Chelton and Xie*, 2010], because stress is enhanced over warmer water and reduced over cooler water. As a result, mesoscale structures such as eddies, fronts, and coastal upwelling systems will induce curl and divergence of surface wind stress [*Pezzi et al.*, 2005; *Chelton et al.*, 2007; *O'Neill el al.*, 2012; *Gaube et al.*, 2013). As we will see next, this is also the case for the wind stress field in the Cap Ghir filament region. Overlaying the QuikScat surface wind field in the Cape Ghir region for 28 August on the closest available SST field (August 27) reveals a clear reduction of wind stress curl intensity over the colder filament waters (Figure 10). The pattern of SST clearly results in a divergence and positive curl of the surface wind stress field (compare Figures 2a and 10). At the filament location, the wind stress field shows a relatively strong cyclonic curl induced by the

Figure 10. Surface wind stress field and corresponding wind curl field for 28 August 2009 as obtained from QuickScat data. The approximate area of positive wind curl induced by the filament is indicated by a blue rectangle.

cool filament waters. A cyclonic wind stress curl band is also clearly recognizable in the offshore upwelling area upstream (north) and downstream (south) the filament. This may also be the result of surface wind stress intensity reduction over upwelled cold water as depicted in Figure 10. *Jin et al.* [2009] found numerically that this SST-induced wind stress curl strengthens offshore upwelling through linear Ekman suction. Their model also indicates that offshore curl-driven upwelling may exceed the coastal upwelling. *Troupin et al.*'s [2012] process-oriented numerical experiments predict that the origin of the Cape Ghir filament is caused by the injection of cyclonic relative vorticity by the linear Ekman suction in the upwelling jet at the offshore boundary of the coastal upwelling. This injected relative vorticity disturbs the potential vorticity balance of the upwelling jet and diverts it from its southward path to turn offshore along zonal contours of positive potential vorticity and thus give rise to the filament. The observed strong cyclonic wind curl at the upwelling jet's location supports this hypothesis. Moreover, the filament's self-induced cyclonic wind stress curl will produce an additional source of cyclonic relative vorticity through linear Ekman suction. This will constrain the filament to be oriented along zonal isolines of potential vorticity although this mechanism may be locally suppressed at the ITE location due to the hypothesized downwelling velocity. The cool filament may also be the result of meridional excursions of the cold filament caused by time-varying wind and eddy forcing, and mixing of the cold filament with the surrounding waters. Therefore, apart from the common wind stress curl forcing, the cold filament region may be also viewed as the active core of the filament and the cool filament as the broader region influenced by it. Self-induced Ekman pumping is however unable to overcome the loss of potential energy associated with the positive density anomaly introduced by the filament in the interior waters. An average value of 10^{-7} N m^{-3} for the wind stress curl over the Cape Ghir filament (Figure 10) will give us a vertical Ekman pumping velocity about $+0.1$ m d^{-1}. If the sub-
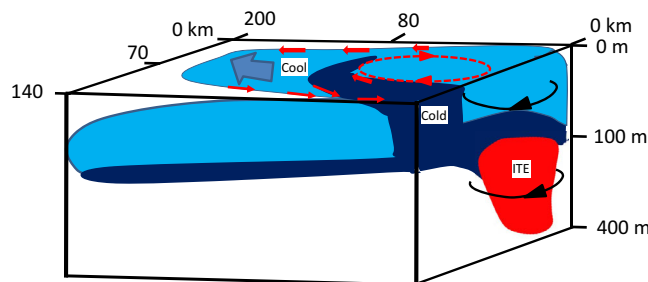

Figure 11. Schematic of the filament components. Dark blue region inner cold filament (cold) embedded in the southern portion of a surrounding larger cool filament (cool). The cold filament interacts with an intrathermocline anticyclonic eddy (ITE), indicated by the red shaded region. Note that the anticyclonic circulation of the ITE reaches the sea surface. Notice also that the cool filament subducts as it extends offshore. The surface circulation in the filament is represented by red arrows. Both cold and cool filaments are bounded by stronger northern seaward jets and weaker southern shoreward jets. The overall offshore flow of the filament is represented by a broad dark blue arrow in the cool filament region.

duction velocity for this filament is similar to that estimated by *Kadko et al.* [1991] in a California Current Upwelling System filament, about -27 m d^{-1}, it is 2 orders of magnitude greater and far from compensated by the self-induced Ekman pumping.

7.3. Comparison With Other Filaments

The observations of the Cape Ghir (CG) filament resemble those of *Ramp et al.* [1991] for the Point Arena (PA) filament in the California Upwelling System. In both cases, the structure consists of a small, shallow, and cold filament embedded within a larger, deeper, cool filament. However, there are several

significant differences. Just north of the cold core of the CG filament, an intrathermocline eddy (ITE) was observed. The anticyclonic velocity field associated with this ITE reaches the surface layers and interacts with the northern front of the filament to strengthen the related offshore jet (Figure 4c). Instead of this ITE-related circulation, *Ramp et al.* [1991] observed for the PA filament a broad offshore outflow related with the cool filament with the cold filament embedded within it. This results in a difference in the relative vorticity distribution in the two cold filaments. In the CG filament case, the cold filament region will be bounded by two narrow jets flowing in opposite directions and strong cyclonic (positive) relative vorticity absent in the PA filament.

In contrast to *Ramp et al.*'s [1991] California Current observations, the inner cold filament off CG does not show intermittency and persists as long as the cool filament, i.e., in every available image. This suggests that both filaments are intimately connected and do not constitute two independent structures as is the case for PA. The difference between CG and PA cold filament characteristics may arise from the different generation mechanisms. *Ramp et al.* [1991] proposed that the PA cool filament was generated by the meandering of the upwelling front, whereas the CG cold filament may be more related with the eddy field and/or with the convergence of coastal currents. In the case of the CG filament, the presence of the ITE may be responsible for generation of the cold filament through two mechanisms. The first relates to the increase of the relative cyclonic vorticity by the ITE and the consequent detachment of the flow from the coast to conserve its potential vorticity as modeled by *Troupin et al.* [2012]. The second mechanism may be the advection of coastal upwelled water by the ITE as suggested by the anticyclonic deflection of the surface chlorophyll signal of the cold filament (Figures 2b and 2d). Generation of the cold filament may be also related to an increase of positive relative vorticity caused by linear Ekman suction, in addition to the effect of the ITE as detailed above. The generation mechanisms of the inner cold and the surrounding cool filament off CG are closely related to each other and to the conservation of potential vorticity.

A high-resolution transect of the cool PA filament reported by *Dewey et al.* [1991] indicates further important differences with the CG filament. First, the PA filament salinity field in the near-surface layers is less homogeneous than in the case of the CG. This may be indicative that in the latter cases, water mass mixing and related secondary circulation are more active. In this regard, *Dewey et al.* [1991] note an offset between the temperature minimum and the considerably narrower salinity maximum. They related this difference between fields to a cross-frontal water exchange linked with the secondary ageostrophic circulation. Our section across the cold filament does not show any offset of temperature and salinity features but the salinity minimum is clearly narrower and the distribution more homogeneous, consistent with active mixing (Figure 6).

A second important difference in the structure is that the offshore jet of the cool PA filament flows geostrophically along the density gradient of its northern front while in the case of CG filament the offshore jet has its axis centered on a bowl-like depression of the isopycnals (Figure 8c). The length scale of this bowl-like structure, $\sim$50 km, is well above the climatological first baroclinic Rossby radius of deformation, $\sim$26 km [*Chelton et al.*, 1998]. If geostrophically adjusted, the bowl structure would relate to an anticyclonic circulation instead of an intense outflow jet. Therefore, in the case of CG, the offshore jet related with the cool filament is strongly ageostrophic. Moreover, below the offshore surface jet, we have observed the signal of a subsurface returning jet (Figures 5a and 5b), a phenomenon not observed in the PA.

The structure of the Cape San Vicente Filament (CSVF), at the southwestern tip of the Iberian Peninsula is composed of a 100 km long, $\sim$44 km wide, and 100 m deep cold filament [*Sánchez et al.*, 2008], but with no evidence of a surrounding larger and deeper cool filament like the CG and PA filaments. Although with lower resolution, a section across the CSVF shows thermohaline and velocity features like the CG system but without any larger surrounding cool filament. In particular, *Sánchez et al.* [2008] found in the northern front of the filament, an anticyclonic circulation that extends to the surface layers to reinforce the offshore filament jet and enhance cyclonic relative vorticity, similar to the CG ITE. However, they suggest that this subsurface structure was related to a small-scale flow meandering associated with a large anticyclone instead of with an ITE. Salinity structure of the CSVF is similar to that for SeaSoar Transect 6 (Figure 6a) in that a salinity minimum was found in the near-surface layers just above the eddy center north of the cold filament boundary. These coincidences between the CG and CSV filament structures suggest that they have a similar generation mechanism where the ITE may play an important role. For both filaments the generation mechanism is most likely related to the conservation of potential vorticity rather than to the meandering of the upwelling front or to the advection of coastal water as proposed for the California Current filaments [e.g., *Strub et al.*, 1991].

8. Conclusions

Our high-resolution observations indicate that the Cap Ghir filament structure is much more complex than concluded on the basis of earlier low-resolution studies. In the summary sketch of the observed situation (Figure 11), the filament comprises three distinct features: (i) a small, shallow, cold filament embedded within, (ii) a larger, deeper cool filament, and (iii) an intrathermocline eddy. The inner cold filament, the location of minimum surface temperature and maximum surface Chl a concentration, is a long (extending 110 km from shore), shallow (60 m deep), and narrow ($\sim$25 km wide) feature bounded by two shallow submesoscale fronts of $\sim$18 km width. The larger surrounding cool filament is warmer than the cold filament but still colder than the background temperatures. It reaches $\sim$200 km offshore, is 120 km wide and 150 m deep and is characterized by a narrow subsurface salinity minimum. The cool filament may be viewed as the broader region influenced by the active cold filament at its core. Both filaments are bounded to their north by fronts, submesoscale in the case of the cold filament and mesoscale for the cool filament. The fronts are associated with relatively intense ($\geq$0.5 m s^{-1}) seaward jets in both cases. Because the cold filament is located at the southern boundary of the surrounding cool filament, their southern fronts are contiguous, but give rise to only a weak ($<$0.15 m s^{-1}) southern shoreward jet. A distinctive feature reported in other filament studies is the occurrence of a deep shoreward return flow ($\leq$0.3 m s^{-1}) below the northern jet. At the head of the cool filament, we observe a 30 m deepening of isotherms and isohalines probably related with its subduction when encountering with warmer more oceanic waters. North of the cold filament, an intrathermocline anticyclonic eddy (ITE) at least 70 km in diameter occupied the depth range of 200–500 m. Similar structures observed at almost the same location in a previous survey of the CG filament [*Pelegrí et al.*, 2005] and also off Cape St. Vincent [*Sánchez et al.*, 2008] are consistent with a link between this structure and the occurrence of the filament.

The reduced surface wind stress was over the CG cold filament and enhancement over warm water downwind the filament results in filament-induced divergence and cyclonic curl of surface wind stress. The additional cyclonic curl will inject further cyclonic relative vorticity to the filament to help maintain its zonal orientation along lines of constant potential vorticity. Independently of the cause of filament generation in other regions, this mechanism may also make an important contribution to their subsequent development and result in the predominantly zonal orientation of filament structures.

Our study reveals that the flow inside the filament is complex, comprising both onshore and offshore flows. The onshore flows may greatly reduce the impact of the overall offshore transport of carbon as well of other biogeochemical properties. *Álvarez-Salgado et al.* [2007] estimated that coastal-ocean transport of organic matter channeled by upwelling filaments might however account for 2.5–4.5 times the offshore carbon export affected by Ekman transport in the Canary Current boundary region. At Cape Juby and Cape Ghir (NW Africa), most of the carbon exchanged by filaments is in dissolved form [*García-Muñoz et al.*, 2004, 2005]. Recirculations associated with these filaments may favor the presence of high surface concentrations of dissolved carbon, and the sinking of particulate material. Additionally, the ITE at Cape Ghir would further enhance sedimentation of particulate organic carbon, increasing the relative proportion of exchanged dissolved material but reducing at the same time the overall amount of total carbon exported to the open ocean.

References

Álvarez-Salgado, X., J. Arístegui, E. D. Barton, and D. A. Hansell (2007), Contribution of upwelling filaments to offshore carbon export in the subtropical Northeast Atlantic Ocean, *Limnol. Oceanogr.*, 52, 1287–1292.

Beardsley, R. C., and S. J. Lentz (1987), The Coastal Ocean Dynamics Experiment collection: An introduction, *J. Geophys. Res.*, 92, 1455–1463.

Bernstein, R. L., L. Breaker, and R. Whritner (1977), California Current eddy formation: Ship, air, and satellite results, *Science*, 195, 353–359.

Brink, K. (1983), The near-surface dynamics of coastal upwelling, *Prog. Oceanogr.*, 12, 223–257.

Brink, K. H., and T. J. Cowles (1991), The coastal transition zone experiment, *J. Geophys. Res.*, 96, 14,637–14,647.

Brink, K. H., D. W. Stuart, and J. C. Van Leer (1984), Observations of the coastal upwelling region near 30′N of California: Spring 198, *J. Phys. Oceanogr.*, 14, 378–391.

Castelao, R. M, and J. A. Barth (2007), The role of wind stress curl in jet separation at a cape, *J. Phys. Oceanogr.*, 37, 2652–2671.

Chelton, D., and S. P. Xie (2010), Coupled ocean-atmosphere interaction at oceanic mesoscales, *Oceanogr. Mag.*, 4, 52–69.

Chelton, D. B., R. A. Deszoeke, M. G. Schlax, K. Naggar, and N. Stwertz (1998), Geographical variability of the first baroclinic Rossby radius of deformation, *J. Phys. Oceanogr.*, 28, 433–460.

Chelton, D. B., M. G. Schlax, and R. M. Samelson (2007), Summertime coupling between sea surface temperature and wind stress in the California Current System, *J. Phys. Oceanogr.*, 37, 495–517.

Collins, C. A., N. Gareld, T. A. Rago, F. W. Rishmiller, and E. Carter (2000), Mean structure of the inshore countercurrent and California undercurrent of Pt. Sur, California, *Deep Sea Res., Part II*, 47, 765–782.

Cornuelle, B. D., T. K. Chereskin, P. P. Niiler, M. Y. Morris, and D. L. Musgrave (2000), Observations and modeling of a California undercurrent eddy, *J. Geophys. Res.*, *105*, 1227–1243.

Dewey R. K., J. N. Moum, C. A. Paulson, D. R. Caldwell, and S. D. Pierce (1991), Structure and dynamics of a coastal filament. *J. Geophys. Res.*, *96*, 14885–1490.

Feldman, G. C., and C. R. McClain (2010), *Ocean Color Web, MODIS Aqua Reprocessing NASA Goddard Space Flight Center*, edited by N. Kuring, and S. W. Bailey. [Available at http://oceancolor.gsfc.nasa.gov.]

Firing, E., J. Ranada, and P. Caldwell, (1985), Processing ADCP Data with the CODAS Software System Version 3.1, *Joint Inst. for Mar. and Atmos. Res./NODC*, Univ. of Hawaii at Manoa, Honolulu.

Flament, P. (1985), The evolving structure of an upwelling filament, *J. Geophys. Res.*, *90*, 11,765–11,778.

Gabric, A. J., L. García, L. van Camp, L. Nykjaer, W. Eifler, and W. Schrimpf (1993), Offshore export of shelf production in the Cap Blanc giant filament as derived from CZCS imagery, *J. Geophys. Res.*, *98*, 4697–4712.

García-Muñoz, M., J. Arístegui, M. F. Montero, and E. D. Barton (2004), Distribution and transport of organic matter along a filament-eddy system in the Canaries–NW Africa coastal transition zone region, *Prog. Oceanogr.*, *62*(2–4), 115–129.

García-Muñoz, M., J. Arístegui, J. L. Pelegrí, A. Antoranz, A. Ojeda, and M. Torres (2005), Exchange of carbon by an upwelling filament off Cape Guir (NW Africa), *J. Mar. Syst.*, *54*, 83–95.

Garfield, N., C. A. Collins, R. G. Paquette, and E. Carter (1999), Lagrangian exploration of the California undercurrent, 1992–1995, *J. Phys. Oceanogr.*, *29*, 560–583.

Garfield, N., M. E. Maltrud, C. A. Collins, T. A. Rago, and R. G. Paquette (2001), Lagrangian flow in the California undercurrent, an observation and model comparison, *J. Mar. Syst.*, *29*(1–4), 201–220.

Gaube, P., D. B. Chelton, P. J. Strutton, and M. J. Behrenfeld (2013), Satellite observations of chlorophyll, phytoplankton biomass and Ekman pumping in nonlinear mesoscale eddies, *J. Geophys. Res. Oceans*, *118*, 6349–6370, doi:10.1002/2013JC009027.

Gordon, A. L., C. F. Giulivi, C. M. Lee, H. H. Furey, A. Bower, and L. Talley (2002), Japan/East Sea intrathermocline eddies, *J. Phys. Oceanogr.*, *32*(6), 1960–1974.

Hagen, E., C. Zülicke, and R. Feistal (1996), Near surface structures in the Cape Ghir filament off Morocco, *Oceanol. Acta*, *19*, 577–598.

Hasegawa, D., H. Yamazaki, R. G. Lueck, and L. Seuront (2004), How islands stir and fertilize the upper ocean, *Geophys. Res. Lett.*, *31*, L16303, doi:10.1029/2004GL020143.

Haynes, R., E. D. Barton, and I. Pilling (1993), Development, persistence, and variability of upwelling filaments off the Atlantic coast of the Iberian Peninsula, *J. Geophys. Res.*, *98*, 22,681–22,692.

Holm-Hansen, O., C. J. Lorenzen, R. W. Holmes, and J. D. H. Strickland (1965), Fluorometric determination of chlorophyll, *J. Cons. Cons. Int. Explor. Mer*, *30*, 3–15.

Hormazabal, S., V. Combes, C. E. Morales, M. A. Correa-Ramirez, E. Di Lorenzo, and S. Nuñez (2013), Intrathermocline eddies in the coastal transition zone off central Chile (31–41°S), *J. Geophys. Res. Oceans*, *118*, 1–11, doi:10.1002/jgrc.20337.

Huyer, A., J. A. Barth, P. M. Kosro, R. K. Shearman, and R. L. Smith (1998), Upper ocean water mass characteristics of the California Current, summer 1993, *Deep Sea Res., Part II*, *45*, 1411–1442.

Ikeda, M., and W. J. Emery (1984), Satellite observations and modeling of meanders in the California Current system of Oregon and Northern California, *J. Phys. Oceanogr.*, *14*, 1434–1450.

Jin, X., C. Dong, J. Kurian, J. C. McWilliams, D. B. Chelton, and Z. Li (2009), SST-windinteraction in coastal upwelling: Oceanic simulation with empirical coupling, *J. Phys. Oceanogr.*, *39*, 2957–2970.

Johnson, G. C., and K. E. McTaggart (2010), Equatorial Pacific 13°C water eddies in the Eastern Subtropical South Pacific Ocean, *J. Phys. Oceanogr.*, *40*(1), 226–236.

Kadko, D. C., L. Washburn, and B. H. Jones (1991), Evidence of subduction within cold filaments of the northern California coastal transition zone, *J. Geophys. Res.*, *96*(C8), 14,909–14,926.

Kelly, K. (1986), The influence of winds and topography on sea surface temperature patterns over the Northern California slope, *J. Geophys. Res.*, *90*, 11,783–11,798.

Kosro, P. M., and A. Huyer (1986), CTD and velocity surveys of seaward jets o northern California, July 1981 and 1982, *J. Geophys. Res.*, *91*, 7680–7690.

Kostianoy, A. G., and I. M. Belkin (1989), A survey of observations on intrathermocline eddies in the world ocean, *in* Mesoscale/Synoptic Coherent Structures in Geophysical Turbulence, Elsevier Oceanogr. Ser., vol. 50, edited by J. C. J. Nihoul and B. M. Jamart, pp. 821–841, Elsevier, Amsterdam, Netherlands.

Lutjeharms, J. R. E., F. A. Shillington, and C. M. Duncombe Rae (1991), Observations of extreme upwelling filaments in the Southeast Atlantic Ocean, *Science*, *253*, 774–776.

Machín, F., A. Hernández-Guerra, and J. L. Pelegrí (2006), Mass fluxes in the Canary basin, *Prog. Oceanogr.*, *70*, 416–447.

Mason, E., F. Colas, J. Molemaker, A. F. Shchepetkin, C. Troupin, J. C. McWilliams, P. Sangrà, and J. L. Pelegrí (2011), Seasonal variability of the Canary Current: A numerical study, *J. Geophys. Res.*, *116*, C00601, doi:10.1029/2010JC006665.

Meunier, T., E. D. Barton, B. Barreiro, and R. Torres (2012), Upwelling filaments off Cap Blanc: Interaction of the NW African upwelling current and the Cape Verde frontal zone eddy field?, *J. Geophys. Res.*, *117*, C08031, doi:10.1029/2012JC007905.

Mooers, C. N. K., and A. R. Robinson (1984), Turbulent jets and eddies in the California Current and inferred cross-shore transports, *Science*, *223*, 51–53.

Nauw, J. J., H. M. van Aken, J. R. E. Lutjeharms, and W. P. M. de Ruijter (2006), Intrathermocline eddies in the Southern Indian Ocean, *J. Geophys. Res.*, *111*, C03006, doi:10.1029/2005JC002917.

O'Neill, L. W., D. B. Chelton, and S. K. Esbensen (2012), Covariability of surface wind and stress responses to sea surface temperature fronts, *J. Clim.*, *25*, 5916–5942.

Pelegrí, J. L., et al. (2005), Hydrographic cruises o northwest Africa: The Canary Current and the Cape Ghir region, *J. Mar. Syst.*, *54*, 39–63.

Peliz, A., A. M. P. Santos, P. B. Oliveira, and J. Dubert (2004), Extreme cross-shelf transport induced by eddy interactions southwest of Iberia in winter 2001, *Geophys. Res. Lett.*, *31*, L08301, doi:10.1029/2004GL019618.

Pérez-Rodríguez, P., J. L. Pelegrí, and A. Marrero-Díaz (2001). Dynamical characteristics of the Cape Verde frontal zone, *Sci. Mar.*, *65*(S1), 241–250.

Pezzi, L. P., R. B. Souza, M. S. Dourado, C. A. E. Garcia, M. M. Mata, and M. A. F. Silva-Dias (2005), Ocean-atmosphere in situ observations at the Brazil-Malvinas confluence region, *Geophys. Res. Lett.*, *32*, L22603, doi:10.1029/2005GL023866.

Ramp, S. R., P. F. Jessen, K. H. Brink, P. P. Niiler, F. L. Daggett, and J.S. Best (1991). The physical structure of cold filaments near Point Arena, California, during June 1987, *J. Geophys. Res.*, *96*(C8), 14,859–14,883.

Sánchez, R. F., P. Relvas, A. Martinho, and P. Miller (2008), Physical description of an upwelling filament west of Cape St. Vincent in late October 2004, *J. Geophys. Res.*, *13*, C07044, doi:10.1029/2007JC004430.

Small, R.J., S. P. deSzoeke, S. P. Xie, L. O'Neill, H. Seo, Q. Song, P. Cornillon, M. Spall, and S. Minobe (2008), Air-sea interaction over ocean fronts and eddies, *Dyn. Atmos. Oceans*, *45*, 274–319.

Strub, P. T., P. M. Kosro, and Huyer (1991). The nature of cold filaments in the California Current system, *J. Geophys. Res.*, *96*, 14,743–14,768.

Troupin, C., E. Mason, J. M. Beckers, and P. Sangrà (2012), Generation of the Cape Ghir upwelling filament: A numerical study, *Ocean Modell.*, *41*, 1–15.

Vélez-Belchi, P., A. Hernández-Guerra, A. Gonzalez-Pola, E. Fraile, C. A. Collins, and F. Machín (2012), The deep Canary poleward undercurrent, Abstract #OS21A-1675 presented at 2012 Fall Meeting, AGU, San Francisco, Calif., Dec.

Zenk, W., B. Klein, and M. Schroder (1991). Cape Verde frontal zone, *Deep Sea Res.*, Part A, *38*(S1), 505–530.